JACS
JOURNAL OF THE AMERICAN CHEMICAL SOCIETY
pubs.acs.org/JACS
Article

Unveiling Dual-Interface Coordination Orchestration for Durable Aqueous Zinc–Iodine Pouch Cells with Four-Electron Chemistry

Yufeng Chen, Renming Liu, Jiahui Hu, Dan Luo, Dongdong Wang,* and Zhongwei Chen*

Cite This: J. Am. Chem. Soc. 2026, 148, 34958–34968
Read Online
ACCESS | Metrics & More | Article Recommendations | Supporting Information

ABSTRACT: Electrolyte additive engineering is regarded as an effective strategy for dual-interface optimization in four-electron aqueous zinc–iodine batteries (AZIBs). However, realizing durable Ah-level AZIBs with industrial-grade parameters (≥10 mg cm^{-2} I_2 cathode mass loading, ≥5 mAh cm^{-2} Zn anode areal capacity) remains a significant hurdle. Here, we compare various nitrogen-containing cationic ligands to evaluate their synergistic regulation on iodine immobilization and Zn nucleation. This screening successfully establishes *N*-methylimidazolium chloride (MImCl) as a premier electrolyte additive for stabilizing dual-interface coordination. Upon discharging, the adsorption of MIm^+ on the I_2 cathode enables electrostatic binding with polyiodides and ICl_2^-. This interaction not only suppresses the polyiodide shuttle but also shields the I^+ species from hydrolysis, promoting a robust and reversible four-electron $I^-/I^0/I^+$ redox chemistry at elevated I_2 mass loading. On the Zn anode, MIm^+ preferentially adsorbs onto its surface during charging, accelerating Zn^{2+} deposition kinetics for dendrite suppression while passivating parasitic reactions, realizing uniform large-capacity Zn plating/stripping. As a result, the engineered 1.4 Ah four-electron Zn||I_2 pouch cells achieve an excellent cyclability of 800 cycles and an ultrahigh cathode-mass-specific energy density of 455 Wh kg^{-1}, surpassing most aqueous Zn-based systems in the Ah-class regime.

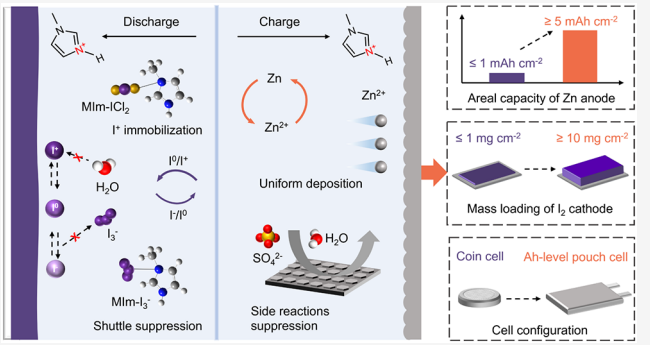

INTRODUCTION

Aqueous zinc metal batteries have emerged as promising candidates for stationary energy storage and micropower systems, capitalizing on their inherent nonflammability, high theoretical capacity (820 mAh g^{-1}; 5855 mAh cm^{-3}), remarkable cost-effectiveness ($ZnCO_3$: 1.1 USD kg^{-1} vs Li_2CO_3: 17 USD kg^{-1}), and excellent environmental compatibility.[1−5] While intercalation cathodes like layered metal oxides and Prussian blue analogues have been widely investigated, their performance is fundamentally constrained by the strong electrostatic interactions of Zn^{2+} with host frameworks, resulting in sluggish ion insertion/extraction kinetics and limited rate capability.[6,7] Moreover, repeated Zn^{2+} insertion and extraction often induce irreversible structural distortion in these crystalline frameworks, leading to progressive capacity fading.[8] In contrast, conversion-type cathodes (S, Se, Te, I_2, Br_2) bypass these limitations through multielectron redox mechanisms with accelerated reaction kinetics.[9−11] Notably, aqueous zinc–iodine batteries (AZIBs) demonstrate particular promise, leveraging earth-abundant iodine resources (~55 μg L^{-1} in seawater) and four-electron redox chemistry.[12] Compared to prevailing Zn-MnO_2 configurations, these four-electron AZIBs exhibit superior metrics, including a high redox potential (~1.8 V vs Zn^{2+}/Zn) and exceptional theoretical capacity (422 mAh g^{-1}).[13,14]

Current implementations of four-electron AZIBs face persistent challenges, namely, parasitic dendrite growth and side reactions for the Zn anode, uncontrolled polyiodide shuttle effects, and hydrolysis of I^+ species for the I_2 cathode, severely compromising cycle life.[15−17] Transitioning toward practical implementation demands systematic scaling strategies, including a Zn anode with industrial-grade areal capacity, a high-loading cathode, and ampere-hour (Ah) scale pouch cell architectures.[18] To date, Zn anode stabilization strategies, including crystallographic orientation control,[19] electrolyte formulation,[20−22] protective interfacial layers,[23,24] and other interfacial engineering approaches, have demonstrated impressive cycling stability by regulating Zn nucleation, promoting uniform Zn^{2+} transport, and suppressing interfacial side reactions. However, these advancements remain confined to coin-cell configurations with limited areal capacity, leaving their effectiveness unproven under industrial-level pouch cells. Similarly, substantial progress has been made in suppressing

Received: June 2, 2026
Revised: July 16, 2026
Accepted: July 20, 2026
Published: August 4, 2026

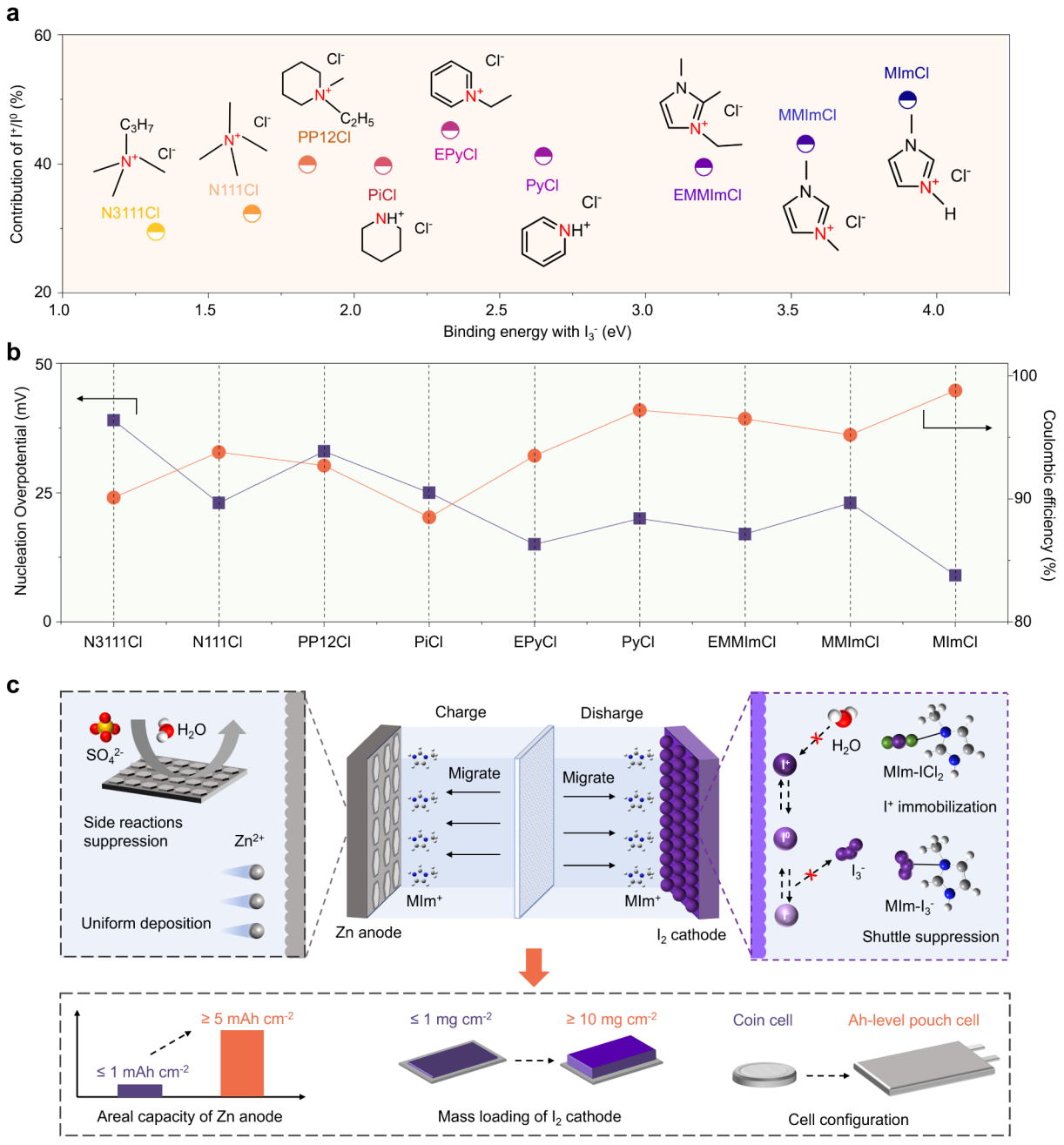

Figure 1. Screening principle and dual-interface coordination for potential additives. (a) Binding energies of I_3^- and additives, and the capacity contribution of I^+/I^0 conversion for various additives. (b) CE and NOP of different additives. (c) Schematic of the dual-interface stabilization enabled by MImCl under the electric field.

the polyiodide shuttle and I^+ hydrolysis in four-electron AZIBs through cathode host engineering,[14] catalytic mediators,[25,26] and electrolyte optimization.[27−29] However, these advancements remain fundamentally constrained by low I_2 mass loadings (typically <1 mg cm^{-2}), failing to meet industrial-grade requirements. Practical Ah-level pouch cells demand high-loading cathode, where amplified polyiodide shuttle and accelerated I^+ hydrolysis trigger intensified Zn anode corrosion ($Zn + I_3^- \leftrightarrow Zn^{2+} + 3I^-$) and aggravated self-discharge from iodine redox imbalance.[30] Concurrently, I_2 dissolution in thick cathodes induces mechanical stress concentration and electrode cracking during cycling, further compromising structural integrity and cyclability. Therefore, developing high-areal-capacity pouch cells inherently demands synergistic optimization of both the Zn anode and the I_2 cathode. Crucial to this endeavor is elucidating the underlying mechanisms by which electrolyte additives stabilize the dual electrochemical interfaces.

Herein, through a systematic investigation and comparison of various nitrogen-containing cationic ligands, we elucidate their synergistic regulation capabilities in anchoring the I_2 cathode and guiding Zn anode nucleation. A novel additive, *N*-methylimidazolium chloride (MImCl), is screened out for electrolyte engineering to simultaneously stabilize the high-areal-capacity Zn anode (≥5 mAh cm^{-2}) and high-mass-loading I_2 cathode (≥10 mg cm^{-2}). Specifically, during discharge, MIm^+ adsorbs on the I_2 cathode, binding to polyiodides and ICl_2^- through ionic interactions. This process

https://doi.org/10.1021/jacs.6c11308
J. Am. Chem. Soc. 2026, 148, 34958−34968

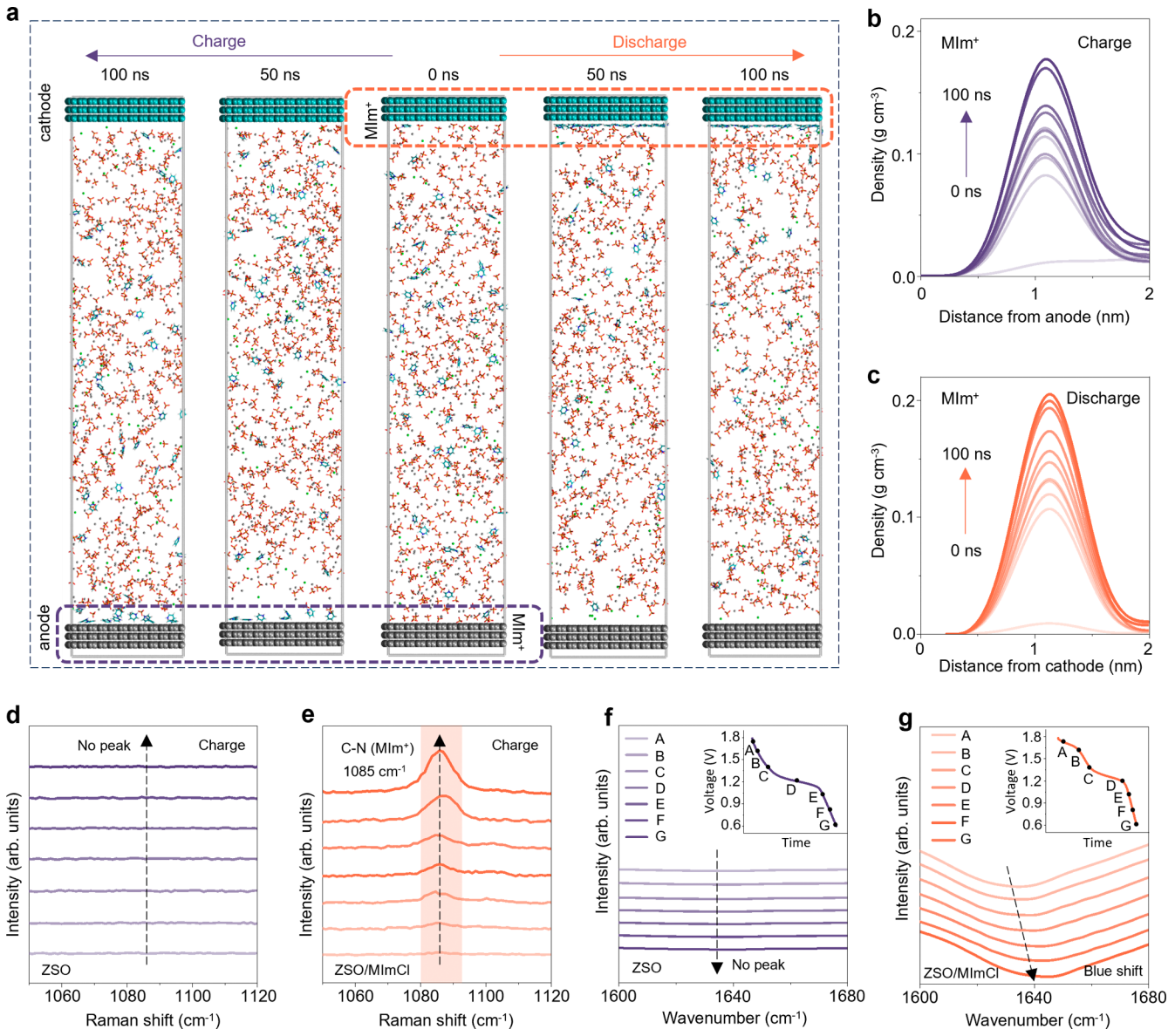

Figure 2. Dynamic absorption of MImCl during the charge/discharge process. (a) MD simulations of ZSO/MImCl during the charge/discharge process. Corresponding MIm^+ distribution at the electrode/electrolyte interface in (b) charge and (c) discharge processes obtained by MD simulations. In situ SERS of the Zn anode surface during the charge process in (d) ZSO and (e) ZSO/MImCl. In situ ATR-FTIR of the I_2 cathode surface during the discharge process from 1.8 to 0.6 V in (f) ZSO and (g) ZSO/MImCl.

effectively suppresses the polyiodide shuttle effect and enhances the stability of the I^+ species against hydrolysis, thereby improving four-electron $I^-/I^0/I^+$ redox reversibility. Upon charging, MIm^+ preferentially migrates to the Zn anode surface, lowering the Zn nucleation potential, which promotes uniform Zn deposition and effectively suppresses side reactions. As a result, the 1.4 Ah four-electron Zn−I_2 pouch cells demonstrate excellent cyclability of 800 cycles and a record energy density of 455 Wh kg^{-1} (based on the mass of the I_2 cathode). This performance outperforms most existing Zn-based energy storage devices in the Ah-class regime. This work establishes a universal interface engineering paradigm for realizing high-capacity four-electron zinc−iodine electrochemistry, accelerating the development of intrinsically safe grid-scale energy storage systems.

RESULTS AND DISCUSSION

Electrolyte Additive Screening Based on Dual-Interface Stabilization

To validate the proposed dual-interface stabilization targeting the I_2 cathode and Zn anode, various nitrogen-containing ionic liquid additives were employed, including quaternary ammonium nitrogen (trimethylamine hydrochloride (N111Cl), propyltrimethylammonium chloride (N3111Cl)), piperidine nitrogen (*N*-ethyl-*N*-methylpiperidinium chloride (PP12Cl), piperidine hydrochloride (PiCl)), pyridine nitrogen (pyridine hydrochloride (PyCl), *N*-ethylpyridinium chloride (EPyCl)), and imidazole nitrogen (*N*-methylimidazolium chloride (MImCl), 1,3-dimethylimidazolium chloride (MMImCl), 1-ethyl-2,3-dimethylimidazolium chloride (EMMImCl)). For the I_2 cathode, selecting suitable additives is crucial for suppressing the polyiodide shuttle and I^+ hydrolysis in four-electron conversion chemistry. As shown in Figure 1a, the binding

https://doi.org/10.1021/jacs.6c11308
J. Am. Chem. Soc. 2026, 148, 34958−34968

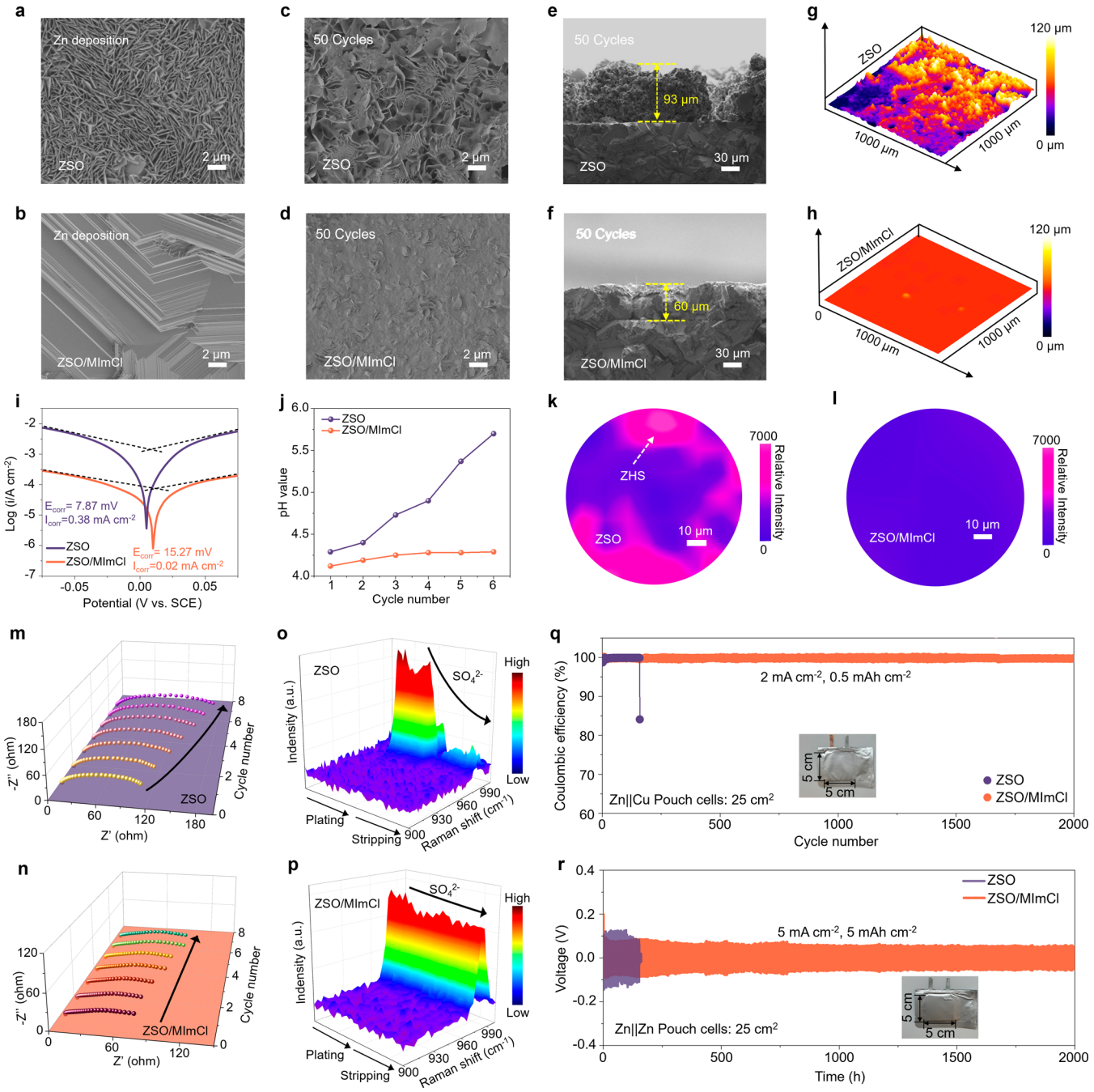

Figure 3. Suppressing Zn dendrites and side reactions on the Zn anode. SEM images of the Zn anode after Zn deposition in (a) ZSO and (b) ZSO/MImCl. Top-view SEM images of the Zn anode after cycling in (c) ZSO and (d) ZSO/MImCl. Side-view SEM images of the Zn anode after cycling in (e) ZSO and (f) ZSO/MImCl. 3D CLSM images of the Zn anode after deposition in (g) ZSO and (h) ZSO/MImCl. (i) LP curves of different electrolytes. (j) In situ pH testing of ZSO and ZSO/MImCl. 2D Raman mapping of the cycled Zn anode in (k) ZSO and (l) ZSO/MImCl. In situ EIS curves of Zn||Zn cells during the charge/discharge process in (m) ZSO and (n) ZSO/MImCl. In situ SERS analysis of SO_4^{2-} intensity change during the plating/stripping process in (o) ZSO and (p) ZSO/MImCl. (q) Cycling performance and CE of Zn||Cu pouch cells using different electrolytes at 2 mA cm^{-2} and 0.5 mAh cm^{-2}. (r) Cycling performance of Zn||Zn pouch cells using different electrolytes at 5 mA cm^{-2} and 5 mAh cm^{-2}.

energy of various cations with triiodide (I_3^-) was investigated via density functional theory (DFT) calculations, with MIm^+ showing the strongest interaction among all cations. The electrostatic potential (ESP) mapping of the cation−I_3^- structures visually corroborates this strong affinity (Figure S1), which is crucial for suppressing the polyiodide shuttle. Furthermore, to address the inherent instability of the I^+ intermediate, the capacity contribution of the I^+/I^0 step was quantified. Notably, with MImCl, this step accounts for 49.8% of the total capacity, the highest value among all additives (Figure S2), demonstrating highly I^+/I^0 conversion devoid of I^+ hydrolysis.[31] For the Zn anode, the initial nucleation overpotential (NOP) and the Coulombic efficiency (CE) of various additives were measured (Figure 1b). MImCl displays a smaller NOP (9 mV) compared to the other additives, reflecting a decreased nucleation barrier for initial Zn^{2+}

https://doi.org/10.1021/jacs.6c11308
J. Am. Chem. Soc. 2026, 148, 34958−34968

deposition (Figure S3). This reduction in nucleation barrier promotes uniform Zn nucleation.[32] The MImCl-modified Zn anode exhibits the highest CE of 99.6% among all additives, attributable to inhibited side reactions and Zn dendrite growth (Figure S4). Collectively, these results confirm the dual-interface stabilization of MImCl, as illustrated in Figure 1c. During the charging process, MIm^+ preferentially migrates to the Zn anode surface and lowers the Zn nucleation overpotential, thereby promoting uniform Zn deposition and effectively suppressing detrimental side reactions. Concurrently, MIm^+ adsorbs onto the I_2 cathode during discharging, immobilizing polyiodides and ICl_2^- anions via strong ionic interactions. This synergistic adsorption effectively mitigates the polyiodide shuttle effect and bolsters the stability of I^+ species against hydrolysis. Guided by this localized electric field, durable Ah-scale four-electron Zn||I_2 pouch cells are demonstrated, delivering a high Zn anode areal capacity (≥5 mAh cm^{-2}) and a practical I_2 cathode mass loading (≥10 mg cm^{-2}).

Electric-Field-Guided Coordination of MImCl at Dual-Electrode Interfaces

The dynamic adsorption of MImCl at the dual-electrode interfaces during the charge/discharge process was investigated by molecular dynamics (MD) simulations. As shown in Figure 2a, during the charge process, MIm^+ undergoes diffusion-driven migration toward the anode under the influence of the built-in electric field. This directional transport induces preferential adsorption at the anode surface (Figure S5). On the contrary, MIm^+ migrates to the cathode under the electric field and leads to MIm^+ accumulation at the cathode surface during the discharge process (Figure S6). Notably, the spatiotemporal evolution of ion distribution reveals distinct migration patterns: during charge, MIm^+ exhibits gradual accumulation of concentration from 0 to 100 ns at the anode surface (Figure 2b), whereas under discharge conditions, its concentration reaches a peak at the cathode interface at 100 ns (Figure 2c). This asymmetric distribution stems from the synergistic effects of electric field-driven migration and concentration gradient-induced back-diffusion. The concentration distribution of Cl^- is also shown in Figure S7. The Cl^- content on the cathode surface increases during the charge process, facilitating the anchoring of I^+ species.

Except for the MD simulations, the dynamic adsorption of MImCl at the dual interfaces during the charge/discharge process was measured by in situ surface-enhanced Raman spectra (SERS) and attenuated total reflection Fourier-transform infrared spectra (ATR-FTIR). In ZSO/MImCl, a peak at 1085 cm^{-1} assignable to the ring-breathing vibration of MIm^+ is observed, whereas it is not detected in ZSO (Figure 2d-e). The time-resolved peak-intensity evolution across applied potentials displays a clear potential-dependent MIm^+ adsorption behavior, suggesting pronounced interfacial accumulation during charging. In situ ATR-FTIR tests were determined on the surface of the I_2 cathode. Compared to ZSO, the C═N stretching vibrations (1630 cm^{-1}) associated with the imidazole ring exhibit distinct spectral evolution in ZSO/MImCl (Figure 2f-g), demonstrating a blue shift and increased intensity during the discharge process from 1.8 to 0.6 V. These changes provide evidence of an increase in MIm^+ concentration near the I_2 cathode surface during discharge. Therefore, the MD simulations and experimental results indicate the potential-directed adsorption of MImCl for dual-interface stabilization.

The effect of MImCl addition on the solvation structure of Zn^{2+} was investigated. X-ray absorption near-edge structure (XANES) analysis of ZSO and ZSO/MImCl resolves Zn^{2+} coordination environments with atomic precision, revealing identical Zn K-edge spectral profiles between both electrolytes, which confirm equivalent ligand coordination configurations (Figure S8). Wavelet transform analysis confirms comparable Zn−O coordination characteristics in both electrolytes, demonstrating that MImCl introduction preserves the original Zn^{2+} solvation configuration without structural modification (Figure S9). FTIR analysis detects congruent S−O (1090 cm^{-1}) and O−H (3250 cm^{-1}) vibrational profiles in both electrolytes (Figure S10). Raman spectra reveal unaltered SO_4^{2-} band positions at 450, 620, and 980 cm^{-1} (Figure S11), while ^1H nuclear magnetic resonance (NMR) confirms null chemical displacement in ZSO and ZSO/MImCl electrolytes (Figure S12). These results collectively demonstrate that the introduction of MImCl, unlike traditional electrolyte additives, does not change the solvation structure of Zn^{2+}.

Suppression of Zn Dendrites and Parasitic Reactions on the Zn Anode

The diffusion kinetics of Zn^{2+} on the Zn surface were investigated. Cyclic voltammetry (CV) curves were carried out to investigate the Zn deposition behavior in Zn||Ti asymmetric cells. As shown in Figure S13, the Zn||Ti cells with ZSO/MImCl exhibit a higher onset potential for Zn plating and a higher current density compared to those with ZSO (|PP"| = 37 mV), indicating improved reaction kinetics owing to the enhanced wetting ability with a decreased contact angle (Figure S14). The addition of MImCl also leads to a higher transference number on the Zn surface than ZSO (0.798 > 0.255) (Figure S15). In addition, the diffusion energy barrier of Zn^{2+} on the Zn anode in ZSO/MImCl is 0.12 eV, much lower than that in ZSO (0.28 eV) (Figure S16), suggesting fast diffusion kinetics, supporting the CV results. Accelerated interfacial diffusion kinetics underpin uniform Zn deposition, as evidenced by scanning electron microscopy (SEM). As shown in Figure 3a, the Zn growth exhibits extreme irregularity in ZSO, where the surface is covered by a large number of thin flakes in random orientations after Zn deposition. In contrast, the plating of Zn in ZSO/MImCl exhibits a directional extension with a uniform and dendrite-free morphology (Figure 3b). The morphology of the Zn anode after cycling in different electrolytes was compared (Figure 3c-d), and cross-sectional SEM images reveal that the Zn anode exhibits a compact and homogeneous microstructure with an average thickness of 60 μm after 50 cycles in ZSO/MImCl, much lower than that in ZSO (93 μm) (Figure 3e-f). This analysis demonstrates the effectiveness of ZSO/MImCl in suppressing Zn dendritic growth while maintaining efficient space utilization. In situ optical microscopy was employed to track the dynamic evolution of Zn deposition. In ZSO, the progressive accumulation of disordered Zn dendrites leads to porous and nonuniform Zn deposition after 60 min. Conversely, it manifests a compact and homogeneous Zn plating process, with no noticeable Zn dendrite formation after 60 min in ZSO/MImCl (Figure S17). The Zn deposition morphology was also analyzed by confocal laser scanning microscopy (CLSM). Figure 3g-h exhibits that the Zn anode surface of ZSO/MImCl is relatively flat with lower roughness

https://doi.org/10.1021/jacs.6c11308
J. Am. Chem. Soc. 2026, 148, 34958−34968

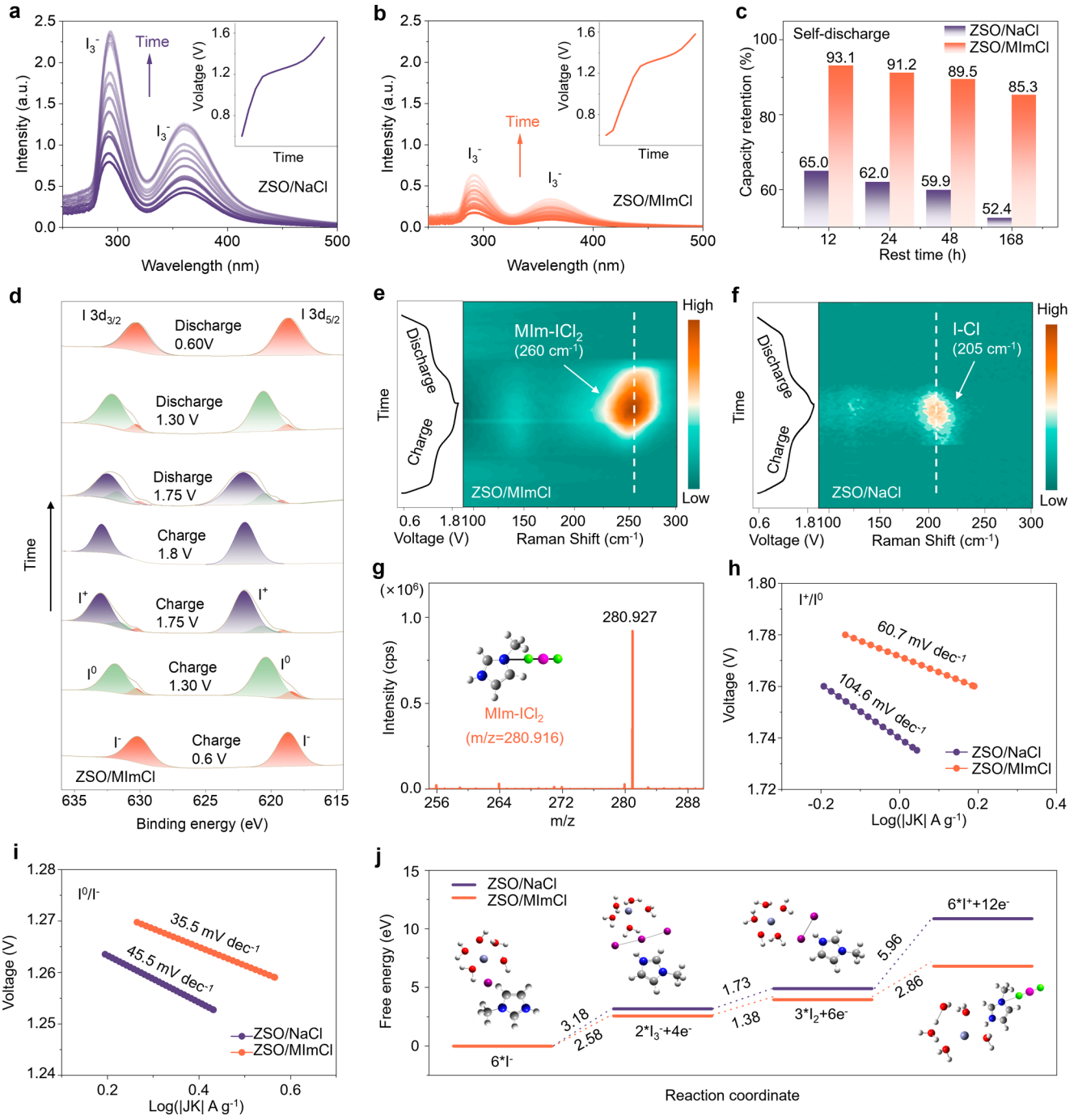

Figure 4. Suppressing the polyiodide shuttle and anchoring I^+ for the I_2 cathode. In situ UV−vis spectra of the I_2 cathode in (a) ZSO/NaCl and (b) ZSO/MImCl during the charging process. (c) Self-discharge performance of Zn||I_2 cells using ZSO and ZSO/MImCl. (d) High-resolution I 3d XPS spectra of the I_2 cathode at different potentials in ZSO/MImCl. Typical galvanostatic voltage profiles and in situ Raman spectra of Zn||I_2 cells using (e) ZSO/MImCl and (f) ZSO/NaCl during the charge/discharge process. (g) MS of the MIm-ICl_2. Tafel slopes of the (h) I^+/I^0 and (i) I^0/I^- reduction peaks. (j) Calculated cohesive energies of I_2 species during the redox routes in ZSO/NaCl and ZSO/MImCl.

compared to that in ZSO. The effect of MImCl on the Zn deposition behavior can be explained by a chronoamperometry (CA) test (Figure S18). Clearly, the Zn plating in ZSO displays continuously increased current density with typical 2D diffusion curves. Such 2D diffusion of Zn^{2+} is more likely to cause inhomogeneous nucleation, which leads to loose and chaotic Zn deposition. Instead, a stable and constant 3D diffusion process occurs in ZSO/MImCl after a short nucleation state of 30 s, indicating that the MImCl additive promotes uniform and smooth Zn growth.

In addition to regulating Zn deposition, the addition of MImCl also inhibits the side reactions on the Zn anode. The linear polarization (LP) curves reveal a positive shift in corrosion potential from 7.87 mV (ZSO) to 15.27 mV (ZSO/MImCl), accompanied by a significant reduction in corrosion current density from 0.38 to 0.02 mA cm^{-2} (Figure 3i). The increased corrosion potential and decreased corrosion current density indicate that MImCl effectively lowers the Zn corrosion reactions. In situ pH monitoring exhibits that the pH value of ZSO increases rapidly from 4.29 to 5.7 during

https://doi.org/10.1021/jacs.6c11308
J. Am. Chem. Soc. 2026, 148, 34958−34968

cycling, originating from severe hydrogen evolution reaction (HER) that triggers localized pH elevation and accelerates parasitic byproduct formation (Figure 3j). In contrast, ZSO/MImCl maintains stable pH values under identical conditions, confirming effective HER suppression (Figure S19). Linear sweep voltammetry (LSV) curves reveal a suppressed onset potential of −0.037 V for ZSO/MImCl, contrasting with 0.181 V for ZSO, demonstrating effective suppression of water reduction reactions (Figure S20). X-ray diffraction (XRD) analysis confirms effective suppression of Zn anode side reactions, with the pristine ZSO electrode showing pronounced $Zn_4SO_4(OH)_6{\cdot}4H_2O$ (ZHS) diffraction peaks, whereas ZSO/MImCl exhibits conspicuously attenuated parasitic ZHS byproduct signatures under identical cycling conditions (Figure S21). Raman spectra corroborate these findings, showing attenuated ZHS signatures at 955 cm^{-1} for Zn anodes in ZSO/MImCl versus the counterpart in ZSO after 100 cycles (Figure S22). Comparative 2D Raman mapping reveals a significant reduction of ZHS accumulation intensity in ZSO/MImCl compared to that in ZSO (Figure 3k-l), confirming effective suppression of parasitic byproduct formation.

Furthermore, in situ electrochemical impedance spectroscopy (EIS) quantitatively evaluates side reactions suppression. The ZSO system exhibits progressive impedance escalation from 99 to 168 kΩ (Figure 3m), mechanistically attributed to the continuous accumulation of insulating byproducts. In stark contrast, ZSO/MImCl maintains stabilized interfacial resistance with <10% fluctuation during cycling (Figure 3n). The sustained low impedance validates mitigated side reactions and dendrite-free Zn deposition, concomitant with preserved electrode integrity. As a critical interfacial species, SO_4^{2-} exhibits dynamic equilibrium during cation storage/release under ideal operation. However, HER-induced OH^- accumulation triggers progressive SO_4^{2-} consumption via ZHS precipitation in ZSO (Figure 3o). This anion depletion induces acute concentration oscillations near the electrode surface, generating localized electric fields that preferentially accelerate Zn^{2+} deposition at protrusions, promoting dendritic growth and cascading parasitic reactions. Conversely, ZSO/MImCl maintains stable SO_4^{2-} concentration profiles, demonstrating effective suppression of this degradation pathway (Figure 3p). Benefiting from uniform Zn deposition and effective suppression of side reactions, the pouch cells display significantly improved cycling stability. As substantiated in Figure 3q, Zn||Cu cells with ZSO demonstrate rapid CE degradation, sustaining merely 158 cycles before failure due to unmitigated parasitic reactions and Zn dendritic propagation. Strikingly, Zn||Cu pouch cells using ZSO/MImCl exhibit exceptional cyclability, maintaining a high average CE of 99.60% over 2000 cycles, representing a 13-fold lifespan enhancement directly attributable to the protection of the Zn anode by MImCl. Complementary evaluation through symmetric Zn||Zn pouch cells (25 cm^2) under 5 mAh cm^{-2} reveals fundamental performance divergences. The Zn||Zn cells using ZSO/MImCl demonstrate unprecedented cycle stability of 2000 h, contrasted by ZSO counterparts undergoing catastrophic failure via dendrite-induced internal short circuits within 160 h (Figure 3r). The Zn||Zn half cells under current densities from 1 mA cm^{-2} to 50 mA cm^{-2} were also compared (Figures S23−S25). This lifespan enhancement quantitatively validates the efficacy of MImCl in stabilizing the Zn anode.

Polyiodide Shuttle Suppression and I^+ Immobilization for the I_2 Cathode

The four-electron AZIBs are fundamentally constrained by the polyiodide shuttle (I_3^-, I_5^-) and I^+ species hydrolysis, challenges that intensify significantly in high-loading I_2 cathode, ultimately resulting in compromised cycling stability. The suppression of the shuttle effect by MImCl was evaluated using in situ UV−vis spectra in a customized quartz cell configuration (Figure S26). In ZSO/NaCl, the absorbance of I_3^- at 290 and 360 nm increases continuously during cycling, indicating significant I_3^- dissolution (Figure 4a). Remarkably, the absorbance diminishes markedly in ZSO/MImCl, demonstrating effective inhibition of the polyiodide shuttle (Figure 4b).[13,33] Self-discharge behavior constitutes a pivotal metric for probing polyiodide shuttle effects (Figure 4c). Zn||I_2 cells with ZSO/NaCl demonstrate capacity retention rates of 72.6% (24 h), 59.6% (48 h), and 53.9% (168 h) during resting (Figure S27). Notably, ZSO/MImCl-modified cells maintain 85.3% capacity retention despite 168 h (7 days), correlating with MImCl-induced suppression of the polyiodide shuttle (Figure S28).

X-ray photoelectron spectroscopy (XPS) analysis of the Zn||I_2 full cell using ZSO/MImCl during cycling was performed to reveal insights into the conversion mechanism (Figure 4d). At the initial resting stage, characteristic peaks for I^- are observed at approximately 619 and 630.5 eV. Upon charging to 1.30 V, peaks indicative of I^0 species emerge at 620 and 632 eV, signifying the formation of I_2. When the voltage increases to 1.75 V, new peaks appear at 622 and 633.5 eV, attributable to activated I^+ species. At the full charge voltage of 1.8 V, iodine is completely converted to I^+. Meanwhile, these transformations show the same trend with high reversibility during the discharge process. In situ Raman spectra reveal discernible I_3^- (110 cm^{-1}) and I_5^- (160 cm^{-1}) vibrational modes across the 1.2−1.8 V operational window in ZSO (Figure S29). In contrast, following the addition of MImCl, the peak intensity of I_3^- and I_5^- is significantly reduced, evidencing effective inhibition of the shuttle effect (Figure 4e). Concomitantly, an emergent 260 cm^{-1} vibrational band emerges at elevated charge/discharge potentials (1.6−1.8 V) in ZSO/MImCl, assigned to stabilized I^+ ions. Notably, these characteristic peaks of I^+ ions exhibit a distinct shift versus conventional ICl benchmarks (Figure 4f),[27,34] indicative of MImCl-mediated coordination environment alterations. Furthermore, to verify the presence of I^+ species, the full cells were disassembled after charging to a high voltage of 1.8 V, and the iodine cathode was subsequently subjected to mass spectrometry (MS) analysis. As shown in Figure 4g, the MS result reveals a characteristic signal corresponding to an MIm-ICl_2 coordination complex (m/z = 280.927), confirming that the introduction of MImCl effectively stabilizes I^+ species via robust coordination interactions.

As shown in Figure 4h and i, the Zn||I_2 full cell using ZSO/MImCl exhibits consistently smaller Tafel slopes for both the I^+/I^0 and I^0/I^- redox couples compared to that with ZSO/NaCl. This reduction in slope indicates accelerated charge-transfer kinetics with diminished activation barriers. This result affirms that MImCl addition significantly boosts the conversion efficiency of the $I^-/I^0/I^+$ redox reactions. Electronic structure analyses through density of states calculations reveal critical coordination differences (Figures S30). The I−Cl system exhibits a molecular orbital energy gap of 2.13 eV, while MIm-ICl_2 coordination demonstrates a 60.6% widening to 3.42 eV.

https://doi.org/10.1021/jacs.6c11308
J. Am. Chem. Soc. 2026, 148, 34958−34968

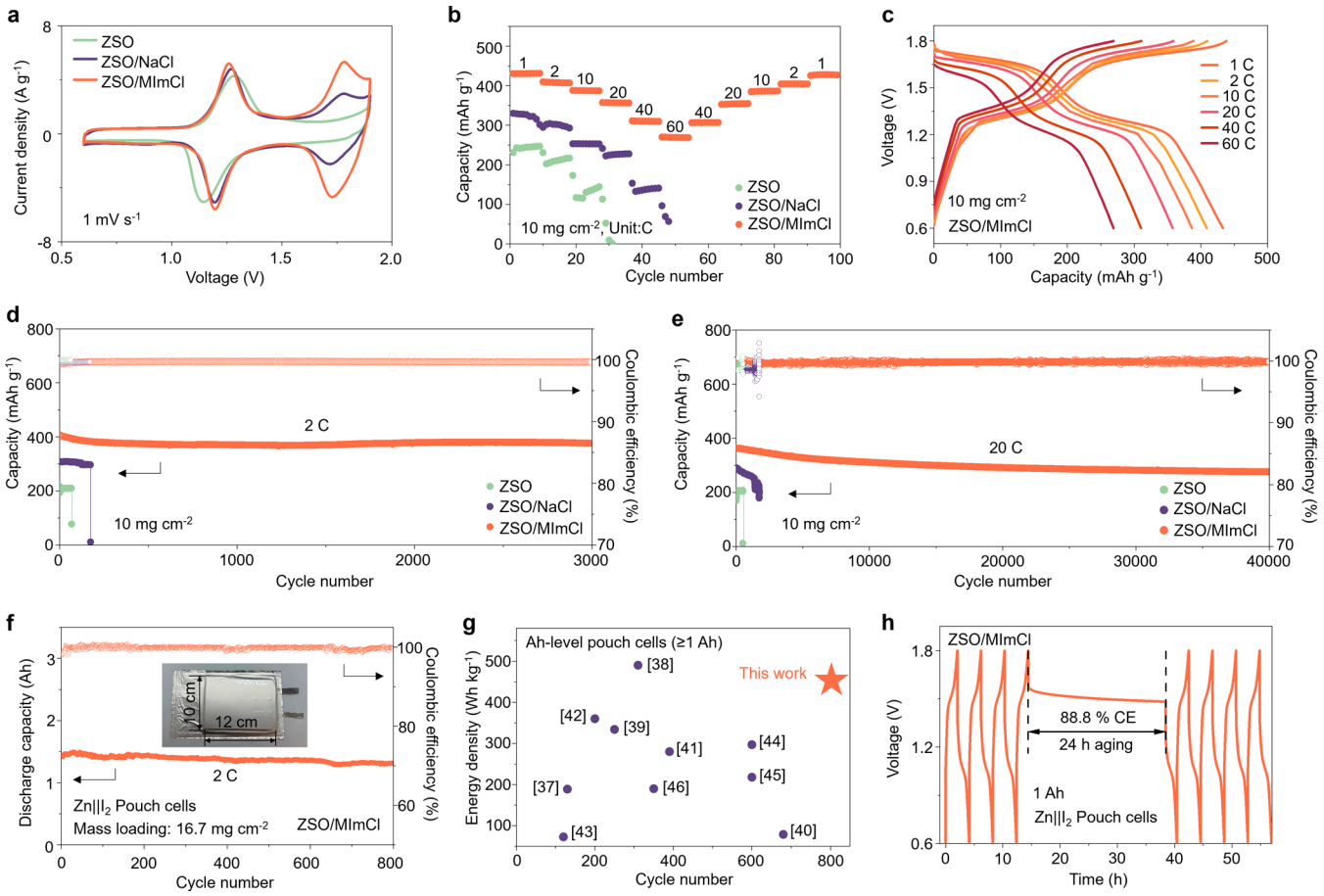

Figure 5. Electrochemical performance of Zn||I_2 full cells. (a) CV curves of Zn||I_2 full cells using different electrolytes at a scan rate of 1 mV s^{-1}. (b) Rate performance of Zn||I_2 full cells using different electrolytes with a high I_2 mass loading of 10 mg cm^{-2} and (c) the corresponding galvanostatic charge/discharge voltage curves. Cycling performance of Zn||I_2 full cells using different electrolytes at (d) 2C and (e) 20C with a high I_2 mass loading. (f) Cycling performance of Ah-level Zn||I_2 pouch cells at 2C. (g) Comparison of the specific energy and cycle life of Ah-level Zn metal pouch cells (≥1 Ah) in published literature and this work (based on the mass of cathode). (h) Self-discharge of Zn||I_2 pouch cells after resting for 24 h at fully charged states.

This quantitative analysis reveals an enhanced dissociation energy for MIm-ICl_2, suggesting that the addition of MImCl strengthens I^+ stabilization through ligand-field reinforcement, thereby establishing a molecular basis for high-valent iodine redox activity. The DFT results demonstrate that the Gibbs free energy change for the oxidation of I_3^- to I_2 in ZSO/MImCl is significantly reduced to 1.38 eV compared to that in ZSO/NaCl (Figure 4j). This thermodynamic finding clearly indicates that ZSO/MImCl effectively promotes the rapid conversion of polyiodides. Furthermore, within the ZSO/MImCl, the transformation of I^0 to I^+ requires overcoming an energy barrier of only 2.86 eV, underscoring a substantial reduction in the reaction energy barrier compared to that in ZSO/NaCl (5.96 eV). Therefore, it is concluded that MImCl not only suppresses the shuttle effect induced by polyiodide during cycling but also anchors I^+ and enhances the reaction kinetics of the $I^-/I^0/I^+$ redox process, enabling robust four-electron redox chemistry for high-performance Zn||I_2 batteries.

Electrochemical Performance of Zn||I_2 Full Cells

ZSO/MImCl was subjected to comprehensive electrochemical evaluation in Zn||I_2 full cells under a high mass loading of the I_2 cathode (Figure S31). The optimal concentration of MImCl was determined by comparing the capacity and CE of Zn||I_2 full cells (Figure S32). CV analysis across electrolyte variants unveils fundamental redox divergences (Figure 5a). ZSO-based cells manifest confined I^-/I^0 redox activity with a complete absence of high-valent iodine species, even at extended polarization (1.9 V). While ZSO/NaCl systems retain residual I^0/I^+ redox capacity, their current response intensity at 1.6−1.8 V remains suboptimal. In stark contrast, ZSO/MImCl-based cells exhibit synchronized dual-redox signatures of robust I^-/I^0 interconversion (1.2/1.4 V) coupled with intensified I^0/I^+ transitions (1.6/1.8 V). This electrochemical contrast directly corroborates the capability of MImCl to stabilize I^+, thereby enabling a distinct four-electron redox signature in full-cell operation. Then, CV profiles of Zn||I_2 full cells using ZSO/MImCl at different scan rates (1−5 mV s^{-1}) and the corresponding capacitive contribution are shown in Figure S33. The preserved peak symmetry and surface-mediated kinetics are observed, confirming stable redox kinetics of the I_2 cathode in ZSO/MImCl. The Zn||I_2 full cells using ZSO/MImCl demonstrate exceptional rate resilience, delivering 420 mAh g^{-1} at 1C and retaining 270 mAh g^{-1} (64.2% capacity retention) at 60C, outperforming those with ZSO/NaCl and ZSO. Remarkably, nearly 100% of the initial capacity (429.6 mAh g^{-1}) is recovered upon reverting to 1C, confirming exceptional electrochemical reversibility (Figure 5b-c). Simultaneously, these cells maintain a higher CE across current densities from 1C to 60C, surpassing control electrolytes

https://doi.org/10.1021/jacs.6c11308
J. Am. Chem. Soc. 2026, 148, 34958−34968

(Figure S34), which directly correlates with MImCl-mediated iodine speciation stabilization and Zn anode passivation synergies. Electrochemical endurance evaluation of Zn||I_2 full cells under high areal loading (10 mg cm^{-2}) exposes electrolyte-dependent degradation pathways. Zn||I_2 full cells employing ZSO/NaCl and ZSO demonstrate accelerated capacity fade with premature failure at ≤200 cycles (Figure S35). The cells using ZSO/MImCl achieve excellent cyclability of 3000 cycles at 2C, delivering a high specific capacity of 400 mAh g^{-1} through stabilized four-electron redox chemistry (Figure 5d). Crucially, these cells maintain CE > 99.5% across 3000 cycles, directly evidencing the inhibitory efficacy of MImCl against polyiodide shuttle and I^+ hydrolysis. Furthermore, at a high rate of 20C, the Zn||I_2 full cell using ZSO/MImCl still exhibits 76% capacity retention after 40000 cycles, highlighting exceptional long-term stability under high-rate operation (Figure 5e).

To substantiate industrial viability, the four-electron Zn||I_2 pouch cells, through monolithic integration of dual-sided I_2 cathode (16.7 mg cm^{-2} active loading per side) with paired Zn foils with thickness of 50 μm, were assembled by precisely controlling the external pressure and interface contact force (Figure S36).[35,36] Capitalizing on the simultaneous electrochemical optimization of four-electron $I^-/I^0/I^+$ redox mediation and Zn anode stabilization by the MImCl additive, the four-electron Zn||I_2 pouch cells utilizing ZSO/MImCl manifest a capacity of 1.4 Ah at 2C and a prolonged cycling life of 800 cycles (Figure 5f). Then, Figure 5g presents a summary of the performance of aqueous Zn metal pouch cells with a capacity exceeding 1 Ah.[37−46] Our study stands out for achieving a high energy density of 455 Wh kg^{-1} (based on the mass of the cathode) and a long cycle life of 800 cycles under Ah-level pouch cell configurations compared to reported data (Table S1). For practical and reliable energy storage, the battery also requires low self-discharge. The Ah-level Zn||I_2 pouch cells using ZSO/MImCl demonstrate a low self-discharge rate of 11.2% after 24 h of resting (Figure 5h). It is worth noting that, compared with conventional two-electron pouch cells,[44,47] this Ah-level four-electron Zn||I_2 pouch cell faces additional challenges associated with I^+ hydrolysis and complex parasitic reactions, making the achieved stable self-discharge performance particularly significant. These analyses highlight a critical breakthrough for implementing four-electron Zn||I_2 chemistry in grid-scale energy storage systems.

CONCLUSIONS

In summary, this work selects a multifunctional electrolyte additive, MImCl, which enables long-life and highly reversible Ah-level four-electron Zn||I_2 pouch cells. During discharge, MIm^+ adsorbs on the I_2 cathode, effectively suppressing the polyiodide shuttle effect and enhancing the stability of the I^+ species against hydrolysis, enhancing four-electron $I^-/I^0/I^+$ redox reversibility under high mass loading. Similarly, the preferential adsorption of MIm^+ on the Zn surface during charging enables uniform Zn deposition, while this modification significantly reduces severe side reactions for large-capacity Zn anodes. Therefore, the Zn||Zn symmetric pouch cells achieve >2000 h of stable cycling under stringent conditions (5 mA cm^{-2}, 5 mAh cm^{-2}). Remarkably, the Ah-level four-electron Zn||I_2 pouch cells deliver a high cathode-mass-based energy density of 455 Wh kg^{-1} and excellent cyclability of 800 cycles, demonstrating a pronounced advantage in existing Zn-based systems in equivalent capacity regimes. This work provides a robust solution for achieving long-life practical Ah-level four-electron Zn||I_2 pouch cells, addressing critical challenges in high-energy aqueous battery design.

ASSOCIATED CONTENT

Supporting Information

The Supporting Information is available free of charge at https://pubs.acs.org/doi/10.1021/jacs.6c11308.

All data needed to evaluate the conclusions in the paper are present. Additional data related to this paper may be requested from the authors. Experimental details, additional characterizations (SEM, XRD, FTIR, Raman, etc.), additional electrochemical tests, and supplementary tables and notes (PDF)

AUTHOR INFORMATION

Corresponding Authors

Dongdong Wang − *State Key Laboratory of Catalysis, Dalian Institute of Chemical Physics, Chinese Academy of Sciences, Dalian 116023, China;* orcid.org/0000-0002-0391-8242; Email: dongdongwang@dicp.ac.cn

Zhongwei Chen − *State Key Laboratory of Catalysis, Dalian Institute of Chemical Physics, Chinese Academy of Sciences, Dalian 116023, China;* orcid.org/0009-0009-9941-3377; Email: zwchen@dicp.ac.cn

Authors

Yufeng Chen − *State Key Laboratory of Catalysis, Dalian Institute of Chemical Physics, Chinese Academy of Sciences, Dalian 116023, China*

Renming Liu − *State Key Laboratory of Catalysis, Dalian Institute of Chemical Physics, Chinese Academy of Sciences, Dalian 116023, China*

Jiahui Hu − *State Key Laboratory of Catalysis, Dalian Institute of Chemical Physics, Chinese Academy of Sciences, Dalian 116023, China*

Dan Luo − *State Key Laboratory of Catalysis, Dalian Institute of Chemical Physics, Chinese Academy of Sciences, Dalian 116023, China*

Complete contact information is available at: https://pubs.acs.org/10.1021/jacs.6c11308

Funding

This work was supported by the Strategic Priority Research Program of the Chinese Academy of Sciences (XDB0600400), the Science and Technology Major Project of Liaoning Province (2024JH1/11700013), DICP Innovation Funding (DICP-I202517), the Vacuum Interconnected Nanotech Workstation (Nano-X), and the Suzhou Institute of Nano-Tech and Nano-Bionics, Chinese Academy of Sciences.

Notes

The authors declare no competing financial interest.

ACKNOWLEDGMENTS

We thank the Shanghai Synchrotron Radiation Facility of BL14W1 (https://cstr.cn/31124.02.SSRF.BL14W1) for the assistance on EXAFS measurements.

REFERENCES

(1) Chu, S.; Majumdar, A. Opportunities and Challenges for a Sustainable Energy Future. *Nature* **2012**, *488*, 294−303.
(2) Meng, Y. S.; Srinivasan, V.; Xu, K. Designing Better Electrolytes. *Science* **2022**, *378*, No. eabq3750.
(3) Albertus, P.; Babinec, S.; Litzelman, S.; Newman, A. Status and Challenges in Enabling the Lithium Metal Electrode for High-Energy and Low-Cost Rechargeable Batteries. *Nat. Energy* **2018**, *3*, 16−21.
(4) Ho, V.-C.; Yen Nguyen Thi, H.; Huong Pham, T.; Jung, H.-G.; Ho Kim, J.; Kim, J. F.; Mun, J. Functional Cellulose Interfacial Layer on Zinc Metal for Enhanced Reversibility in Aqueous Zinc Ion Batteries. *Chem. Eng. J* **2024**, *496*, 153845.
(5) Li, Y.; Liu, X.; Zhang, M.; Sheng, D.; Ren, P.; Che, L.; Wang, X.; Shen, Z. X. Optimization Strategy of Surface and Interface in Electrolyte Structure of Aqueous Zinc-Ion Battery. *ACS Mater. Lett* **2024**, *6*, 1938−1960.
(6) Park, H.; Bartel, C. J.; Ceder, G.; Zapol, P. Layered Transition Metal Oxides as Ca Intercalation Cathodes: A Systematic First-Principles Evaluation. *Adv. Energy Mater* **2021**, *11*, 2101698.
(7) Wang, L.; Liu, N.; Li, Q.; Wang, X.; Liu, J.; Xu, Y.; Luo, Z.; Zhang, N.; Li, F. Dual Redox Reactions of Silver Hexacyanoferrate Prussian Blue Analogue Enable Superior Electrochemical Performance for Zinc-Ion Storage. *Angew. Chem., Int. Ed* **2025**, *64*, No. e202416392.
(8) Zeng, X.-X.; Zhang, S.; Long, T.; Zhao, Q.-Y.; Wang, H.-R.; Ling, W.; Wu, X.-W.; Yu, A.; Chen, Z. An Amphipathic Ionic Sieve Membrane for Durable and Dendrite-Free Zinc-Ion Batteries. *Renewables* **2024**, *2*, 52−60.
(9) Yin, Y.; Li, X. Review and Perspectives on Anodes in Rechargeable Aqueous Zinc-Based Batteries. *Renewables* **2023**, *1*, 622−637.
(10) Li, G.; Sun, L.; Zhang, S.; Zhang, C.; Jin, H.; Davey, K.; Liang, G.; Liu, S.; Mao, J.; Guo, Z. Developing Cathode Materials for Aqueous Zinc Ion Batteries: Challenges and Practical Prospects. *Adv. Funct. Mater* **2024**, *34*, 2301291.
(11) Chen, Z.; Zhi, C. Chalcogens for High-Energy Batteries. *Nat. Rev. Mater* **2025**, *10*, 268−284.
(12) Zhong, W.; Cheng, H.; Zhang, S.; Li, L.; Tan, C.; Chen, W.; Lu, Y. Cation-Driven Phase Transition and Anion-Enhanced Kinetics for High Energy Efficiency Zinc-Interhalide Complex Batteries. *Nat. Commun* **2025**, *16*, 4586.
(13) Zou, Y.; Liu, T.; Du, Q.; Li, Y.; Yi, H.; Zhou, X.; Li, Z.; Gao, L.; Zhang, L.; Liang, X. A Four-Electron Zn-I_2 Aqueous Battery Enabled by Reversible $I^-/I_2/I^+$ Conversion. *Nat. Commun* **2021**, *12*, 170.
(14) Wang, C.; Ji, X.; Liang, J.; Zhao, S.; Zhang, X.; Qu, G.; Shao, W.; Li, C.; Zhao, G.; Xu, X.; et al. Activating and Stabilizing a Reversible Four Electron Redox Reaction of I^-/I^+ for Aqueous Zn-Iodine Battery. *Angew. Chem., Int. Ed* **2024**, *63*, No. e202403187.
(15) Lin, D.; Li, Y. Recent Advances of Aqueous Rechargeable Zinc-Iodine Batteries: Challenges, Solutions, and Prospects. *Adv. Mater* **2022**, *34*, 2108856.
(16) Yu, H.; Wang, Z.; Zheng, R.; Yan, L.; Zhang, L.; Shu, J. Toward Sustainable Metal-Iodine Batteries: Materials, Electrochemistry and Design Strategies. *Angew. Chem., Int. Ed* **2023**, *62*, No. e202308397.
(17) Chen, H.; Li, X.; Fang, K.; Wang, H.; Ning, J.; Hu, Y. Aqueous Zinc-Iodine Batteries: From Electrochemistry to Energy Storage Mechanism. *Adv. Energy Mater* **2023**, *13*, 2302187.
(18) Zhang, M.; Sun, C.; Chen, G.; Kang, Y.; Lv, Z.; Yang, J.; Li, S.; Lin, P.; Tang, R.; Wen, Z.; et al. Synergetic Bifunctional Cu-In Alloy Interface Enables Ah-Level Zn Metal Pouch Cells. *Nat. Commun* **2024**, *15*, 9455.
(19) Li, Z.; Beyene, T. T.; Zhu, K.; Cao, D. Realizing Fast Plating/Stripping of High-Performance Zn Metal Anode with a Low Zn Loading. *J. Met., Mater. Miner* **2024**, *34*, 2009.
(20) Yang, C.; Woottapanit, P.; Hou, Q.; Dai, Z.; Limphirat, W.; Qin, J.; Zhang, X. Self-Separating Biphasic Electrolyte Enables High-Performance Aqueous Zinc-Ion Batteries via Electron-Enriched Interphase Engineering. *Nano Micro Lett* **2026**, *18*, 367.
(21) Yang, C.; Woottapanit, P.; Zhang, X.; Qin, J. Recent Advances in Hydrogel Polymer Electrolytes for Stable Zinc Metal Anodes. *Chem. Commun* **2026**, *62*, 1409−1426.
(22) Tang, J.; Dai, Z.; Yang, C.; Chanajaree, R.; Okhawilai, M.; Pattananuwat, P.; Rajendran, S.; Zhang, X.; Qin, J. Breaking the Water Activity Barrier: Hydrated Eutectic Electrolytes for Long-Cycling and Wide-Temperature Zinc-Ion Batteries. *Adv. Funct. Mater* **2026**, *36*, No. e15911.
(23) Woottapanit, P.; Yang, C.; Geng, S.; Lolupiman, K.; Limphirat, W.; Zhang, X.; He, G.; Qin, J. Electron Donation Effect of α-Boron Nanosheet Enables Highly Stable Zinc Metal Anode. *Adv. Funct. Mater* **2025**, *35*, No. e2507725.
(24) Tanapornchinpong, P.; Yang, C. W.; Zhao, Y. H.; Kiatwisarnkij, N.; Lolupiman, K.; Rajendran, S.; Lei, Y. P.; Zhang, X. Y.; Wangyao, P.; Qin, J. Q. Enhanced Zn Plating and Stripping Behavior of the Utilized Fly Ash-coated Zn Anode for Zinc-Ion Batteries. *Rare Met* **2025**, *44*, 4621−4630.
(25) Liu, T.; Lei, C.; Wang, H.; Xu, C.; Ma, W.; He, X.; Liang, X. Practical Four-Electron Zinc-Iodine Aqueous Batteries Enabled by Orbital Hybridization Induced Adsorption-Catalysis. *Sci. Bull* **2024**, *69*, 1674−1685.
(26) Guan, D.; et al. π-d Conjugated Coordination Mediated Catalysis for Four-Electron-Transfer Fast-Charging Aqueous Zinc-Iodine Batteries. *Matter* **2025**, *8*, 101932.
(27) Zong, W.; Li, J.; Zhang, C.; Dai, Y.; Ouyang, Y.; Zhang, L.; Li, J.; Zhang, W.; Chen, R.; Dong, H.; et al. Dynamical Janus Interface Design for Reversible and Fast-Charging Zinc-Iodine Battery under Extreme Operating Conditions. *J. Am. Chem. Soc* **2024**, *146*, 21377−21388.
(28) Lyu, Y.; Yuwono, J. A.; Wang, P.; Wang, Y.; Yang, F.; Liu, S.; Zhang, S.; Wang, B.; Davey, K.; Mao, J.; et al. Organic PH Buffer for Dendrite-Free and Shuttle-Free Zn-I_2 Batteries. *Angew. Chem., Int. Ed* **2023**, *62*, No. e202303011.
(29) Wang, M.; Meng, Y.; Sajid, M.; Xie, Z.; Tong, P.; Ma, Z.; Zhang, K.; Shen, D.; Luo, R.; Song, L.; et al. Bidentate Coordination Structure Facilitates High-Voltage and High-Utilization Aqueous Zn-I_2 Batteries. *Angew. Chem., Int. Ed* **2024**, *63*, No. e202404784.
(30) Yue, Q.; Wan, Y.; Li, X.; Zhao, Q.; Gao, T.; Deng, G.; Li, B.; Xiao, D. Restraining the Shuttle Effect of Polyiodides and Modulating the Deposition of Zinc Ions to Enhance the Cycle Lifespan of Aqueous Zn-I2 Batteries. *Chem. Sci* **2024**, *15*, 5711−5722.
(31) Li, W.; Xu, H.; Zhang, H.; Wei, F.; Zhang, T.; Wu, Y.; Huang, L.; Fu, J.; Jing, C.; Cheng, J.; et al. Designing Ternary Hydrated Eutectic Electrolyte Capable of Four-Electron Conversion for Advanced Zn-I_2 Full Batteries. *Energy Environ. Sci* **2023**, *16*, 4502−4510.
(32) Liu, T.; Lei, C.; Wang, H.; Li, J.; Jiang, P.; He, X.; Liang, X. Aqueous Electrolyte With Weak Hydrogen Bonds for Four-Electron Zinc−Iodine Battery Operates in a Wide Temperature Range. *Adv. Mater* **2024**, *36*, 2405473.
(33) Xu, W. Y.; Chang, Z. L.; Wang, H. W. Competitive solvent occupation chemistry enabling robust four-electron conversion for anti-freezing aqueous zinc−iodine batteries. *Energy Environ. Sci* **2026**, *19*, 3010.
(34) Yu, W. B.; Wang, X. Y. Dual-Electrode Stabilization of Aqueous Zinc-Iodide Batteries Enabled by an Amino-Functional Imidazolium Bromide Additive. *Adv. Funct. Mater* **2026**, *36*, No. e75185.
(35) Oh, H.; Kim, J. T.; Shin, H.-J.; Kim, A. Y.; Bak, C.; Kim, S.-O.; Chung, K. Y.; Mun, J.; Kim, J.; Lee, Y. M.; et al. Stable Performance for Pouch-Type All-Solid-State Batteries Enabled by Current Collector with Optimized Primer Layer. *Mater. Sci. Eng., R* **2025**, *164*, 100970.
(36) Koo, J. K.; Yun, Y.; Seo, J. K.; Ha, S. H.; Kim, D. W.; Mun, J.; Kim, Y.-J. Detrimental Electrochemical Behavior Caused by Excessive High Pressure on Li-Ion Pouch-Type Full Cell. *Electrochem. Commun* **2023**, *152*, 107518.
(37) Lin, C.; Zeng, L.; Liu, M.; Xiao, F.; Lin, H.; Chen, L.; Lu, Y.; Qian, Q.; Chen, Q.; Zhang, K.; et al. Dynamic Regulation for the

https://doi.org/10.1021/jacs.6c11308
J. Am. Chem. Soc. 2026, 148, 34958−34968

Well-Distribution of Electrons and Zn^{2+} Ions Achieving Uniform Zn Redox in Ah-Scale Pouch Cells. *Adv. Mater* **2025**, *37*, No. e11484.
(38) Guo, H.; Luo, H.; Zhu, F.; Li, S.; Su, X.; Chen, Z.; Liu, A.; Li, J.; Zhou, W.; Lu, M.; et al. Mechanical-Thermal Decoupling Engineering Unlocks Ultra-Stable Dry Thick Iodine Cathodes for Ah-Level Zinc-Based Pouch Batteries. *Adv. Mater* **2026**, *38*, No. e73037.
(39) Hu, X.; Dong, H.; Gao, N.; Wang, T.; He, H.; Gao, X.; Dai, Y.; Liu, Y.; Brett, D. J. L.; Parkin, I. P.; et al. Self-Assembled Polyelectrolytes with Ion-Separation Accelerating Channels for Highly Stable Zn-Ion Batteries. *Nat. Commun* **2025**, *16*, 2316.
(40) Song, Y.; Chen, M.; Zhong, Z.; Liu, Z.; Liang, S.; Fang, G. Bilateral In-Situ Functionalization towards Ah-Scale Aqueous Zinc Metal Batteries. *Nat. Commun* **2025**, *16*, 3142.
(41) Hu, Y.; Zhang, S.-J.; Wu, H.; Chen, Q.; Zhang, P.; Hao, J.; Qiao, S.-Z. A Water-Responsive Molecule Realizes Stable Ah-Scale Zn-I_2 Pouch Cells with High Zn Utilization. *Energy Environ. Sci* **2026**, *19*, 1551.
(42) Wang, F.; Zhang, J.; Lu, H.; Zhu, H.; Chen, Z.; Wang, L.; Yu, J.; You, C.; Li, W.; Song, J.; et al. Production of Gas-Releasing Electrolyte-Replenishing Ah-Scale Zinc Metal Pouch Cells with Aqueous Gel Electrolyte. *Nat. Commun* **2023**, *14*, 4211.
(43) Zheng, X.; Han, B.; Cheng, S.; Liu, S.; Wang, F.; Wu, Y. Molecular Armor Encapsulation of Practical Layered Cathode Empowers Energetic Ah-Level Zn-MnO_2 Pouch and Prismatic Cells. *JACS Au* **2025**, *5*, 4904−4915.
(44) Zhang, S.-J.; Hao, J.; Wu, H.; Hu, Y.; Chen, Q.; Johannessen, B.; Ma, Q.; Luo, D.; Qiao, S.-Z. Electroactive Ferrocene/Ferrocenium Redox Coupling for Shuttle-Free Aqueous Zinc-Iodine Pouch Cells. *Nat. Chem* **2026**, *18*, 266−274.
(45) Li, C.; Min, J.; Zhang, X.; Zhao, S.; Qu, G.; Yu, Q.; Yang, M.; Yuan, D.; Xu, X. Efficient $I^-/I_3^-/I_2$ Conversion and Shuttle-Suppression in High-Rate Ah-Level Zinc-Iodine Batteries Enabled by Bifunctional Confined-Catalyst ZrB_2/AC Host. *Angew. Chem., Int. Ed* **2026**, *65*, No. e9794577.
(46) Zhang, S.-J.; Hao, J.; Wu, H.; Chen, Q.; Hu, Y.; Zhao, X.; Qiao, S.-Z. Coordination Chemistry toward Advanced Zn-I_2 Batteries with Four-Electron $I^-/I^0/I^+$ Conversion. *J. Am. Chem. Soc* **2025**, *147*, 16350−16361.
(47) Wu, H.; Hao, J.; Zhang, S.; Jiang, Y.; Zhu, Y.; Liu, J.; Davey, K.; Qiao, S. Z. Aqueous Zinc-Iodine Pouch Cells with Long Cycling Life and Low Self-Discharge. *J. Am. Chem. Soc* **2024**, *146*, 16601−16608.

https://doi.org/10.1021/jacs.6c11308
J. Am. Chem. Soc. 2026, 148, 34958−34968